THE ASTROPHYSICAL JOURNAL, 454:15–31, 1995 November 20

ACTION PRINCIPLE SOLUTIONS FOR GALAXY MOTIONS WITHIN 3000 KILOMETERS PER SECOND

EDWARD J. SHAYA
Department of Physics, University of Maryland, College Park, Maryland 20742
P. J. E. PEEBLES
Theoretical Astrophysics 130-33, California Institute of Technology, Pasadena, California; and Physics Department, Princeton University, Princeton, NJ 08544
AND
R. BRENT TULLY
Institute for Astronomy, University of Hawaii, Honolulu, HI 96822
Received 1994 December 21; accepted 1995 June 2

ABSTRACT

If we could reconstruct the orbits that galaxies followed to arrive at their present observed positions and velocities, there is much we would learn about the distribution of mass and the initial conditions of fluctuations. A discussion of how to achieve this reconstruction is begun here. The analysis requires a redshift catalog of mass tracers. The numerical action variational principle is used to find fully nonlinear solutions for the orbits of the mass tracers given their present redshifts and angular positions and the cosmological boundary condition that the peculiar velocities are small at high redshift. A solution predicts the distances of the mass tracers and is tested by a comparison with measured distances. The current numerical results use 289 luminosity–line width distance measurements designed to be close to unbiased. A catalog of 1138 tracers approximates the luminosity distribution of galaxies in the vicinity of the Local Supercluster, at redshifts $cz < 3000$ km s^{-1}. These mass tracers include groups with crossing times less than the Hubble time and isolated galaxies. In this preliminary computation, we assign each mass tracer the same mass-to-light ratio M/L. The tracer masses are fixed by apparent magnitudes and model distances. The only two free parameters in this model are M/L and the expansion time t_0. The measure of merit of a solution is the sum of the mean square differences between the predicted and observed distance moduli. In the 3000 km s^{-1} sample, this reduced χ^2 statistic has a well-defined minimum value at $M/L = 175$ and $t_0 = 10.0$ Gyr, and χ^2 at the minimum is about 1.29 times the value expected from just the standard deviation of the distance measurements. We have tested for the effect of the mass at greater distance by using the positions of Abell clusters as a model for the large-scale mass distribution. This external mass model reduces the minimum value of χ^2 by about 10% (approximately 1 σ). The value of the cosmological density parameter Ω_0 is determined by the global mean mass-to-light ratio. Our preliminary analysis yields $\Omega_0 = 0.17 \pm 0.10$ at 1 σ. A tighter bound is expected to come out of a larger sample of measured distances now available.

Subject headings: cosmology: observations — dark matter — galaxies: clusters: general — galaxies: distances and redshifts — methods: numerical

1. INTRODUCTION

This analysis of the deviations from homogeneous Hubble flow involves four steps: (1) establish a catalog of positions and redshifts of objects that represent the present-day mass distribution; (2) solve for orbits of these mass tracers that result in their present angular positions and redshifts; (3) measure distances to a sample of the mass tracers; and (4) use a statistical measure of the differences between the observed distances and the distances in the orbit solution to optimize the free parameters. The program combines previous discussions of the galaxy distances and redshifts (Shaya, Tully, & Pierce 1992, hereafter STP92; Tully, Shaya, & Pierce 1992, hereafter TSP92) and a numerical method of computation of the orbits (Peebles 1989, 1990, 1994, hereafter P89, P90, and P94, respectively). Our purpose for this paper is to present the considerations that lead to our choices of the astronomical and numerical techniques and to show some first numerical results from the analysis of the observations.

Numerical solutions to the N-body problem in step (2) require six independent constraints on the orbit of each mass tracer. In a Robertson-Walker line element, three of the constraints can be set by the assumption that the peculiar velocities were negligible compared to the rates of expansion between nearest neighbors at earliest times. Two additional constraints can be set by the present location of tracers in the plane of the sky, and the last constraint can be the observed redshift. These three observables can be measured to high accuracy. Theoretically, then, if one had a complete and accurate catalog of mass tracers out to a reasonable distance, with positions in celestial coordinates, redshifts, and masses, and one knew the age of the universe, one would know the discrete set of possible galaxy orbits since formation. In the process, one would predict the present distances and transverse velocities. The action variational principle of classical mechanics is readily adapted to the computation of orbits given locations in the sky plus distances. This method has been applied to the Local Group of galaxies and its immediate neighbors (P89; P90; P94; Dunn & Laflamme 1993). In § 2.1 we describe a

modification that determines the orbits and predicts the present distances given the present redshifts.

We do not have the perfect catalog just described, of course, and there are two main obstacles to creating it. First, the zone of avoidance causes optical catalogs to be incomplete. We describe in § 3.1 the use one can make of observations in the infrared and radio to provide information on the galaxy distribution at low Galactic latitudes. Our conclusion is that the zone of avoidance is a diminishing problem. Second, nonluminous mass need not cluster with the galaxies. If the dark mass has low pressure, it is very likely that the mass clusters with the galaxies on large scales because the gravitational instability of the expanding universe draws galaxies and dark matter together in the same way. If so, the issue would be the scale of significant segregation of galaxies and dark mass. We argue in § 6.2 that if galaxies and mass were significantly segregated on scales of a few megaparsecs, we would expect to detect the effect in the relative motions of the galaxies in and near the Local Group. A mass component with a broader coherence length might be present and might be detected by a study of the relative motions of the more widely separated mass tracers. There also is the very real possibility that galaxies in denser regions have larger mass-to-light ratios, meaning there is a mass component that is more tightly clustered than the galaxies. Clearly, much remains to be learned from modeling the relation between starlight and the underlying mass.

Step (3) in the program requires a distance measure that is unbiased or has biases one understands and can remove. In § 4 it is explained why we think our biases are minimal. Differences of observed and predicted distance moduli provide a measure of the fit of the model to the observations, and we apply the luminosity–line width (Tully-Fisher) method in a way that is expected to yield unbiased estimates of individual distance moduli with a standard deviation $\delta\mu \sim 0.4$, independent of distance. This uncertainty $\delta\mu$ is in reasonable agreement with the residuals found in the numerical fit in § 5, an indication that we have a statistical measure of goodness-of-fit that behaves in a well-understood way.

The main result of the computation is the measure of a χ^2 fit as a function of the independent parameters. In the model we focus on here, the cosmological constant vanishes and all mass tracers have the same mass-to-light ratio M/L, so the independent parameters are M/L and the expansion time t_0. There are two independent parameters rather than the single parameter that appears in some studies because we do not assume that the mean density of our sample agrees with the cosmic mean (or, equivalently, that the mean rate of expansion of the sample agrees with the background Hubble flow). Rather, as a secondary product that does not govern the fit, we derive the mean density of the sample and find that it is close to the cosmic mean when the parameters are close to the minimum of χ^2. The relevant parameter from the cosmological model is t_0 because, in the absence of a cosmological constant or other smoothly distributed component in the stress-energy tensor, time is the only locally observable cosmological parameter. If this simplicity seems unexpected, recall that in general relativity theory local physics is unaffected by the expansion of the universe except insofar as the expansion sets the time t_0.

To summarize this important point: rather than work in the domain of mass perturbations on a mean density and peculiar velocities upon a mean Hubble expansion, we consider total masses that act over a specified time to generate global observed velocities.

2. THE ACTION VARIATIONAL PRINCIPLE METHODOLOGY

The numerical action procedure in P89, P90, and P94 yields orbits with given present positions for the mass tracers treated as point particles. The position of each tracer as a function of time is supposed to trace the motion of the center of mass of the components out of which it is assembled, and it is assumed that the gravitational effect of these components on the motion of other mass elements at high redshift is well approximated by replacing the distributed mass with the single particle at the center of mass. Some tests of this picture are discussed in § 6.2.

The mass tracers have comoving positions $x_i(t)$. The equation of motion, assuming a matter-dominated universe with negligible nongravitational forces throughout the relevant time span, can be derived from the paths at extrema and saddle points of the action,

$$S = \int_0^{t_0} \left[\sum \frac{m_i a^2}{2} \left(\frac{dx_i}{dt} \right)^2 + \frac{G}{a} \sum_{i \neq j} \frac{m_i m_j}{|x_i - x_j|} + \frac{2}{3} \pi G \bar{\rho} a^2 \sum m_i x_i^2 \right] dt , \quad (1)$$

where $\bar{\rho}$ is the background density.

We plan to consider two families of cosmological models: those with zero cosmological constant Λ and those with a nonzero Λ set such that the universe has zero space curvature. The latter is consistent with most interpretations of inflation as an explanation of the large-scale homogeneity of the observable universe. A model with nonzero values of both Λ and space curvature seems more unlikely because it would require a double coincidence of the epochs of life on Earth, the transition of the expansion rate to curvature dominance, and the transition to Λ dominance.

In the two families of models, time intervals are

$$H_0 \, dt = \frac{a^{1/2} da}{[\Omega_0 + a^p (1 - \Omega_0)]^{1/2}} , \quad (2)$$

where $p = 1$ if $\Lambda = 0$, and $p = 3$ if the model is cosmologically flat. In most of the numerical results presented in this paper we assume $\Lambda = 0$, but we mention some trials that indicate the cosmologically flat model would yield quite similar results with larger expansion times.

The orbits are approximated by parametric functions:

$$x_i^\alpha(t) = x_i^\alpha(t_0) + \sum_n C_{i,n}^\alpha f_n(t) , \quad (3)$$

where α denotes the spatial component and the f_n are a set of functions satisfying the boundary conditions. The choice is not critical; we use

$$f_n = (1 - a)^{s-n} a^n \left[\frac{s!}{n!(s-n)!} \right] , \quad 0 \leq n < s . \quad (4)$$

The solutions to the equation of motion occur where the gradients with respect to the coefficients of the trial function vanish,

$$\frac{\delta S}{\delta C_{i,n}^\alpha} = 0 . \quad (5)$$

In general, there may be many solutions consistent with the boundary conditions. We choose the mass tracers by grouping galaxies into systems that are not likely to have crossed, so, apart from the classical triple-valued regions, the interesting

solution is the minimum of the action. We find this minimum by walking down the gradient of the action until the sum of the squares of the gradients is below a target three or four orders of magnitude below the value in an initial trial that had all coefficients set to zero and the distances set to the initial guesses discussed below.

2.1. *Iterations to Observed Redshifts*

The only three well-determined phase-space coordinates in large catalogs are the two coordinates of projected positions and the radial velocities; distances are at best only approximately known. We know of two ways to adapt the algorithm to predict distances given redshifts. A variational method (P94) requires a matrix inversion that seems impractical for a large sample. The alternative used here finds present distances given the redshifts by the following iterative procedure. The first step is to make initial guesses for the distances of the tracers and solve for the orbits. The orbit solutions in general are not acceptably close to the given velocities. Therefore, the local gradients in the model velocities with respect to the given present distances are determined numerically. All of the distances along the lines joining mass tracers and the Local Group are adjusted from the initial guesses by positive 0.1 Mpc. After this small distance change, new solutions are calculated. For each mass tracer, the small change in model redshift is compared to the difference between model and observed redshift, and an estimate is made of the distance shift that will bring the model in line with the observed redshift. The actual distance adjustment is the smaller of half the estimated shift or 1 Mpc. Limiting the distance steps in this way prevents overshoot to qualitatively new configurations in any one step, which is important to prevent jumps to new branches of multiple-value regions.

The procedure is repeated with increasing accuracy by decreasing the target value of the sum of the squares of the gradients. After about 10 iterations there is usually excellent agreement between calculated and observed redshifts for all but one or two mass tracers. The exceptions usually are tracers that have been caught at a triple-value region and need to get beyond it. An increase in the minimum step size for one iteration near the end of the computation usually lets these tracers escape and then resettle at a better location.

2.2. *Numerical Details*

A softening parameter in the inverse square force law is set to 10^{-2} times the sample radius or $c = 30$ km s^{-1} $= 0.3\ h^{-1}$ Mpc. The force softening is useful in the initial iterations, but after the mass tracers have nearly settled to their final paths c may be reduced to zero with no significant consequences since there are no close interactions in this sample, by design (see § 3.1).

To check the orbit solutions from the action principle we use a conventional N-body code to integrate the motions forward in time from initial positions and velocities taken from the earliest time step in the action variational solution. We use 90 time steps in this integration. Good agreement between the N-body and action orbits are normally found for five parameters ($s = 4$ in eq. [4]). As to be expected, when there are still small errors in the early time motion, perhaps because the target value for the sum of the squares of the gradients has not been set low enough, the present positions from the N-body code may be quite different from the true values. Yet the action principle solution usually is reasonably accurate. This test therefore requires one to calculate to greater precision in the action method than one really cares, but it is worth the effort to have an accurate N-body confirmation.

We ran additional tests with the mass-to-light ratio set to $M/L = 1$ because that case can be checked analytically. Because M/L is so small, this case is equivalent to free Hubble expansion in a region that is empty save for test particles of negligible mass. One trial used a background cosmological model with $\Omega_0 = 0.6$ and $\Lambda = 0$, and in another trial Λ was set to make the universe cosmologically flat. All 1138 particles were used in these tests. The velocities of particles were within approximately 1% of theoretical expectations.

For 1138 mass tracers, there are $1138 \times 5 \times 3 = 17{,}070$ coefficients to vary to minimize the action. The integrals are calculated with 30 time steps, resulting in approximately 3% accuracy for peculiar velocities. Trials show that every factor of 3 increase in the number of time steps results in a factor of 2 increase in precision. With our set of parameters, a typical solution for given present positions takes 1 hr with a DEC AXP workstation. The project began with earlier and slower workstations, however, and approximately 2000 CPU hours on various workstations have been expended on the calculations here and on tests of robustness and accuracy.

2.3. *Scaling Laws*

We use two scaling relations. These results assume we can neglect nongravitational forces and the cosmological constant Λ. They can also be useful approximations when the universe is cosmologically flat and $\Lambda \neq 0$.

The first relation is the simple result that the solutions for the orbits of particles of specified masses, which follow proper physical positions $r(t)$ relative to the center of mass as functions of proper time t and end up at given present positions $r(t_0)$, depend only on the expansion time, t_0. This condition follows from Birkoff's theorem: in a region with radius small compared to the Hubble length, the interactions of the particles may be described using Newtonian mechanics (with a tidal field from the external mass fluctuations). The background cosmological model serves only to set the value of t_0. Peculiar velocities relative to the global expansion do depend on Ω_0 as well as t_0, of course, because the expansion rate in the background cosmological model is determined by H_0.

The conclusion is that any cosmological model for which H_0 and Ω_0 imply a given t_0 predicts the same relation between mass tracer distances and redshifts. In our action computations we use a standard nominal value of the Hubble constant and a range of values of Ω_0 chosen to produce the desired range of values of t_0. We have checked that the action variational solutions based on different combinations of H_0 and Ω_0 that give the same t_0 do give the same relations between the mass tracer redshifts and distances.

A goal of this program is the analysis of the effect of large-scale mass fluctuations on the reconstruction of the orbits of the nearer mass tracers. Since the fluctuations on very large scales have small density contrast $\delta\rho/\rho$, it is efficient and reasonable to represent their effect on the nearer mass tracers by an applied tidal gravitational field that is a given function of comoving position and with amplitude that grows with time according to linear perturbation theory. To the extent that this treatment is a good approximation in the cosmological model with the nominal values of H_0 and Ω_0, it is also a good approximation to the predicted distances in any other model with the same value of t_0 and $\Lambda = 0$.

The second relation is a gravity scaling law. Suppose we have a set of comoving positions $\boldsymbol{x}_i(t)$ for all particles in a solution to an N-body problem with pure gravitational interactions, and consider a rescaling of proper times, comoving positions, and masses by the equations

$$t' = t/\alpha\ , \quad \boldsymbol{x}'(t') = \beta \boldsymbol{x}(t) = \beta \boldsymbol{x}(\alpha t')\ , \quad m' = \gamma m\ , \tag{6}$$

where α, β, and γ are constants. If the expansion parameters in the original and scaled cosmological models satisfy the relation

$$a'(t') = a(t) = a(\alpha t')\ , \tag{7}$$

then the cosmological acceleration equation is

$$\frac{\ddot{a}'}{a'} = -\frac{4}{3}\pi G\rho' = -\frac{4}{3}\pi G\rho\gamma\beta^{-3} = \alpha^2\frac{\ddot{a}}{a}\ , \tag{8}$$

from which we see that the scaling parameters satisfy

$$\gamma = \alpha^2\beta^3\ . \tag{9}$$

The Hubble constants in the original and scaled model satisfy $H_0' = \alpha H_0$; the mass density scales as $\rho' = \alpha^2\rho$; the density parameters are unchanged ($\Omega_0' = \Omega_0$); the luminosity derived from given apparent magnitudes scales as $L' = \beta^2 L$; and the mass-to-light ratio scales as $M'/L' = \alpha^2\beta M/L$. Finally, one readily checks that the scaled orbits $\boldsymbol{x}'(t')$ satisfy the same equation of motion as the original orbits $\boldsymbol{x}(t)$.

We use two applications of this scaling relation. First, the scales of time and mass in our numerical results are set by observed redshifts and the length scale of the luminosity–line width distances. If further progress in the calibration of the length scale were to adjust the luminosity–line width distances by the factor β, as in equation (6), then since the velocities are not changed we would have $\alpha = \beta^{-1}$, meaning expansion times and masses scale in proportion to the length scale.

Second, we can reduce the number of cases to compute with the action principle, because the solutions for various mass-to-light ratios at a given expansion time t_0 can be scaled to other values of t_0. To hold the redshifts fixed, we adjust α with $\beta = \alpha^{-1}$. In practice, though, only a limited range in M/L is interesting at each value of t_0, and it is often the case that the range of values explored at one choice of t_0 do not rescale into the interesting range at some other value of t_0. Rather, the benefit is that we can calculate a coarse grid of parameter values and then use scaling to fill in interesting parts of the grid at higher resolution. As a check, we have used the rescaling to determine distances at dramatically different values of t_0 and fixed velocities, and we compared the results to direct action variational computations at the new values of t_0 and M/L. The results agree to a few percent, with the exception of a mass tracer in a triple-value region that jumped to a very different orbit.

3. INPUT DATA

The model predicts distances and masses of objects in a catalog of mass tracer redshifts, positions on the sky, and luminosities, with the only free parameters being t_0 and M/L. This catalog is supplemented by initial guesses of distances that serve to speed convergence of the computation and discriminate among alternative possibilities when the solution is not unique, as in triple valued regions. The influence of density fluctuations on scales greater than 3000 km s^{-1} is modeled by a set of positions of "external masses." Finally, we match M/L for the mass tracers to the global mean value to determine H_0 and Ω_0 in terms of t_0 and M/L. In this section we discuss the choices of all these quantities.

3.1. *The Catalog of Mass Tracers at cz < 3000 Kilometers per Second*

The mass tracer catalog is an extension of the one used in the linear analysis by STP92 and given in Table 2 of TSP92. That earlier description of the local distribution of galaxies and light was derived from the Nearby Galaxies (NBG) catalog (Tully 1988a). The "associations" defined by Tully (1987) constituted the mass tracers in TSP92. The current extension introduces three significant modifications.

1. Galaxies in unbound associations are handled differently. It was appreciated that the linear analysis in STP92 was inaccurate in high-density regions, so the mass tracers were grouped at the low-luminosity threshold of the "associations" in the terminology of Tully (1987). We can venture into higher density regions with the present analysis. In principle, the action computation can be applied in situations in which the crossing time is short, although ambiguities arise because we have no way to choose among the many extrema and saddle points of the action. We want to avoid these complications in this preliminary study and have therefore chosen to group galaxies into mass tracers that should not have experienced a close passage with any other tracer. That is, we aim to construct the catalog so that the crossing times between mass tracers are greater than t_0.

This condition is just the group identification criterion in Tully (1987). In that earlier study, groups were identified on the basis of a luminosity density threshold. It was demonstrated that the chosen threshold produced a group catalog with characteristic crossing times less than or comparable to the age of the universe. Hence, for the present study each Tully group is counted as a single mass tracer. Galaxies in Tully associations are below the luminosity density threshold and enter the catalog as several mass tracers. To be rigorous, we must note that there are some "associations" in the Tully (1987) group analysis above the luminosity density threshold but that are tidally sheared by an adjacent massive cluster. Since such an entity can have a short crossing time, the galaxies within it are consolidated as a single mass tracer for the present study. Each mass tracer is assigned the average velocity and angular position of its constituent galaxies. In this paper the averages are number weighted; in future papers we plan to consider the effect of luminosity weighting.

2. A substantial improvement to the low-latitude coverage is implemented with the merging of information from the *IRAS* 1.2 Jy survey (Fisher 1992; Fisher et al. 1992). The improvements are in two parts. First, there is greater completion to low latitudes, with uniform density maintained down to a latitude of 5°. Second, we have a new procedure to deal with the equatorial band, where there is almost no information. The NBG catalog was meant to have uniform all-sky coverage, within the constraints of Galactic obscuration. The uniform, all-sky *IRAS* 1.2 Jy sample provides an important supplement.

All 1304 *IRAS* 1.2 Jy sources with galactocentric velocities less than 3000 km s^{-1} are used in the updated database. Of these, 836 were already in the NBG catalog, and 468 are new. The new objects are either at low Galactic latitudes or at high velocities (>1500 km s^{-1}), where the NBG catalog is known to be incomplete. A new *IRAS* galaxy is integrated into an existing mass tracer from the NBG catalog if it is within $2\,h^{-1}$ Mpc ($h = H_0/100$) of a tracer member in the appropriate sum of

angular position and velocity (where the differential radial distances are taken to be $0.01c\,\Delta z\,h^{-1}$ Mpc). *IRAS* sources within $2\,h^{-1}$ Mpc of each other and not incorporated in NBG tracers are grouped into a new mass tracer, or isolated *IRAS* sources become themselves a new tracer.

The vast majority of *IRAS* sources have blue magnitudes in the Third Reference Catalogue of Bright Galaxies (de Vaucouleurs et al. 1991). We apply the standard NBG catalog Galactic and inclination absorption adjustments to incorporate these new objects into our database. In only 38 highly obscured cases are there no blue magnitudes. In these cases, magnitudes are constructed from our *IRAS* count normalization (1 *IRAS* count $= 2 \times 10^{10} L_B \times f_{IRAS}$, where f_{IRAS} is a distance incompletion factor that grows in a slightly nonlinear way from unity at 1300 km s^{-1} to 2.5 at 3000 km s^{-1}).

The treatment of the Galactic plane was unsatisfactory in the STP92 analysis, and the new treatment to be described now represents a major improvement of the current catalog. The solid histogram in Figure 1 illustrates the distribution of known galaxies in the merged NBG catalog and *IRAS* sample, in $\sin|b|$ bins (where b is Galactic latitude). The histogram would be flat for a uniform galaxy distribution and fair sampling. It is seen that the characteristics of our sample are consistent with this proposition for $\sin|b| > 0.09$ ($|b| > 5°$). The *IRAS* survey is impressively complete, at least within the restricted velocity range $V_0 < 3000$ km s^{-1}.

At $|b| < 5°$ (9% of the sky) our merged catalog is highly incomplete. We want to maintain a uniform luminosity density, so *fake* mass points are created according to the following recipe. All real catalog mass tracers with $5° < b < 15°$ create a tracer with the same distance and longitude but at latitude $b_{\rm fake} = b_{\rm real} - 10°$. All real tracers with $-15° < b < -5°$ reflect to a tracer with $b_{\rm fake} = b_{\rm real} + 10°$. Each fake tracer is assigned half the luminosity of its progenitor. By construction, the luminosity in $\sin|b|$ bins at $|b| < 5°$ is consistent with that at higher latitudes (*dashed histogram* in Fig. 1). Structure is diluted by the halving of individual luminosities and the blending by reflections from each side of the Galactic plane.

3. Many new distance measurements are becoming available, including quite a few to galaxies that are not in the NBG or *IRAS* catalogs. In future studies we will use these data in the goodness-of-fit measure, so the galaxies have been added to the mass tracer catalog by the procedure used in introducing the *IRAS* 1.2 Jy sources. Again, these new galaxies all have redshifts $cz > 1500$ km s^{-1}, where the NBG catalog is incomplete.

The mass tracer catalog sample has been corrected for residual incompleteness as a function of distance following the procedure in Tully (1988b), but since the updated sample includes 28% more galaxies, the correction is smaller. The catalog is truncated at $M_B^{b,i} = -16^{\rm m}$. At input distances less than 10 Mpc, there is no correction for incompleteness. At larger distances, the mass tracer luminosities are multiplied by a correction factor that varies nonlinearly from $F_L^{\rm new} = 1$ at 10 Mpc to $F_L^{\rm new} = 2.4$ at 35 Mpc. In STP92 and TSP92 the maximum value of the correction factor was $F_L^{\rm old} = 3.0$.

There are 1323 mass tracers in the catalog in its present form. Of these, 847 consist of a single galaxy. The largest tracers are the Virgo Cluster, with 157 galaxies, and the Hydra I and Centaurus clusters at the edge of the sample with comparable luminosities. Figure 2 is a histogram of the number of tracers in bins of log luminosity. Some of the tracers have quite low luminosities. In the present computation we have applied a luminosity cutoff at $3 \times 10^9\ L_\odot$ for tracers without distance measurements, but we keep all tracers with measured distances. The resulting 1138 tracers are used in the computations discussed in § 5.

We also use a set of initial guesses for the mass tracer dis-

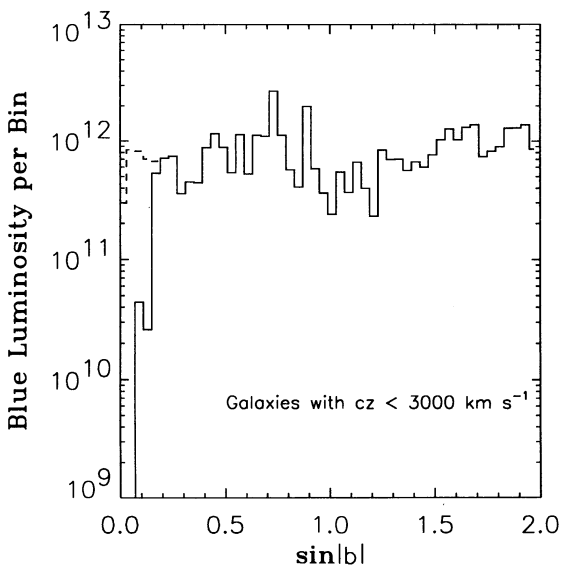

FIG. 1.—The distribution of blue light associated with galaxies in $\sin|b|$ bins (where b is Galactic latitude; bin increments are 0.02 in $\sin|b|$). The solid histogram represents the 3030 galaxies in the merged NBG catalog and *IRAS* sample. The dashed histogram illustrates the situation with the inclusion of 151 "fake" entries at $|b| < 5°$. Appropriately, there is rough constancy of luminosity in $\sin|b|$ bins in the combined data set of real plus fake mass tracers.

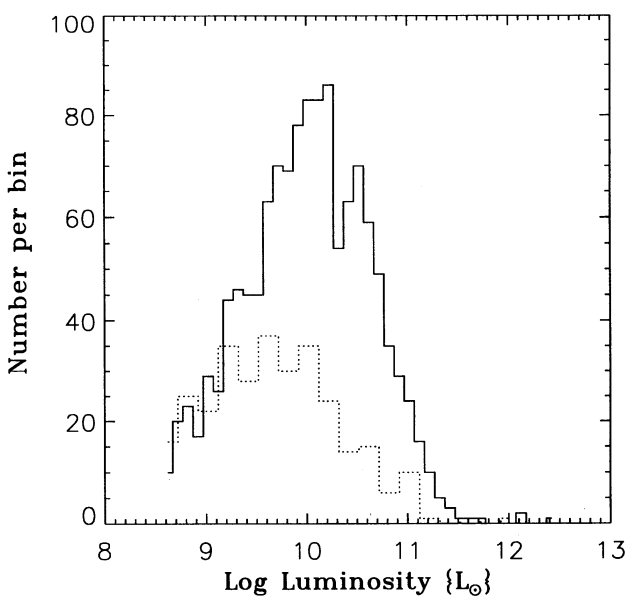

FIG. 2.—Histogram of the number of mass tracers per luminosity bin. Solid histogram is based on the entire catalog. There is a sharp turnover because of incompleteness at the faint end and because the objects at large cz are boosted in luminosity by the correction factor. Orbits are calculated for mass tracers with $L_B^{b,i} > 5 \times 10^9\ L_\odot$ and/or with measured distances. The dotted histogram is restricted to $cz < 1500$ km s^{-1} and $|b| > 30°$, where the catalog is more nearly complete and the corrections for luminosity are small. The turnover at $10^9\ L_\odot$ is probably due to residual incompleteness.

tances. For most of the mass tracers the action solution is unique, but with reasonable initial approximations to the distances fewer iterations are required to generate good solutions. If there is more than one solution for a given velocity, then the computation will tend to find the solution with distance nearest the input value. Hence, in regions where triple-value zones are suspected, such as around the Virgo Cluster, we use measured distances when available to discriminate between alternative input distance choices. For the other mass tracers the initial distance estimates are in statistical agreement with the subset with measured luminosity–line width distances, and we invoke continuity of filamentary structures on the plane of the sky and in velocity. The same recipe was used in our earlier linear analysis (STP92; TSP92). The initial trial distance assignment for a new mass tracer from the *IRAS* sample is the distance of the nearest neighboring NBG tracer multiplied by the ratio of the redshifts of the new and NBG tracers.

The solution is tested against a subset of mass tracers with measured distances. In the examples presented here, we use the TSP92 list of distances, excluding nine mass tracers. Five galaxies give distances well removed from the predictions of all models (worse than 8 σ). These five distance measurements provide no model discrimination, probably are bad data, and so are removed. One group is near the edge of the sample with a few member galaxies beyond the velocity cutoff and must therefore be removed. Finally, three mass tracers very near the Virgo Cluster are thought to be caught in the middle of the triple-value region. However, in models with low constant M/L, the triple-value region does not go out far enough to include these galaxies. We will later detail how these objects indicate a greater than nominal mass-to-light ratio for the Virgo Cluster. This leaves us with 289 galaxies providing velocity independent distance measures to 186 mass tracers.

3.2. *Beyond 3000 Kilometers per Second*

Our redshift catalog of mass tracers represents the nearby region at $cz < 3000$ km s^{-1}, which encompasses the historical Local Supercluster. However, it is generally appreciated that this region is significantly affected by mass fluctuations on larger scales (Lilje, Yahil, & Jones 1986; Dressler et al. 1987; Strauss et al. 1992; STP92). Here we describe a way to explore the effect.

It is too time consuming at present to compute the orbits of the mass tracers at $cz > 3000$ km s^{-1}. Rather, we fix these distant tracers in comoving coordinates and scale the amplitude of their gravitational field as a function of time according to linear perturbation theory. We call the mass tracers treated this way "external masses"; they are external to the volume with reconstructed orbits. As noted in § 2.3, if $\Lambda = 0$, this procedure can be applied in a background cosmological model with any combination of H_0 and Ω_0 that yields the wanted t_0.

There are two useful descriptions of the large-scale distributions of objects: the *IRAS* and Abell catalogs. We use the QDOT *IRAS* sample (Rowan-Robinson et al. 1990) and the sample of Abell clusters from Lauer & Postman (1994). The two are similar enough that they both induce a flow of the nearby mass tracers in the general direction of the apex of the thermal cosmic background radiation dipole, and they both generate a quadrupole tide along an axis running from Hydra-Centaurus to Perseus. The method is illustrated in this paper by an external mass model based mainly on the Lauer-Postman clusters.

Lauer & Postman (1994) identified 128 clusters that they show are likely to be a complete sample at high Galactic latitudes and within 15,000 km s^{-1}. It is known that the northern component (Abell 1958) is deficient in richness class zero clusters compared with the southern component (Abell, Corwin, & Olowin 1989), but Lauer & Postman argue that this deficiency should not affect the sample at $z < 0.05$ because such fairly nearby clusters are easily identified. We use the relative distance estimates that Lauer & Postman obtained for 120 of the clusters.

The distribution of the Lauer-Postman sample in latitude is shown in Figure 3. Incompletion apparently sets in rather abruptly at $|b| = 24°$ ($\sin|b| = 0.4$). There should be 80 clusters at $|b| < 24°$ to maintain a uniform density, where only eight are known. This 48° equatorial gap is much greater than the 10° gap in the *IRAS* 1.2 Jy sample, so a different technique is used to fill in the missing clusters. The *IRAS* 0.6 Jy 1 in 6 sparse-sampled (QDOT) survey (Rowan-Robinson et al. 1990) has been provided for us in a binned format (Kaiser et al. 1991). We are given an irregular grid with the ratio of observed counts in cells to the counts expected for a homogeneous distribution. We use the lowest latitude bins, $10° < |b| < 32°$. An "equivalent cluster count" is created with the product of the normalized *IRAS* count in the cell times the bin volume size times a bin normalization factor. The bin normalization factor is chosen to get the right overall number of sources in the equatorial $\sin|b|$ bins of Figure 3. Then the "equivalent cluster count" is assigned a position, not at the center of the bin, but displaced to the edge of the bin at $|b| = 10°$, in order to fill the empty zone $-24° < b < 24°$ with two bin strips with centers at $b = \pm 10°$. As a matter of detail, the "equivalent cluster counts" are fractional and are smaller nearby, because the bin volumes are smaller, so we are not placing any unduly large masses nearby. The assignment of these fake clusters has some observational motivation, but they reflect the distribution of *IRAS* galaxies rather than clusters, and the *IRAS* galaxy distribution observed at $10° < |b| < 32°$ is taken to represent the distribution in the offset interval $0° < |b| < 24°$.

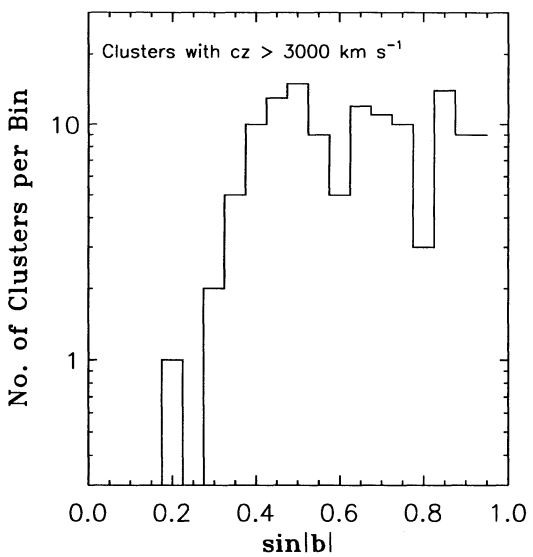

FIG. 3.—The histogram of the Lauer-Postman sample of Abell clusters in $\sin|b|$ bins (bin increments are 0.05 in $\sin|b|$). "Fake" sources are generated from information provided in the low latitude distribution of the QDOT 0.6 Jy *IRAS* survey but cannot sensibly be plotted in this figure because they are all located in the single bin associated with $b = \pm 10°$.

The computations in § 5 with external masses use this augmented cluster sample. The net mass in the region occupied by the set of clusters and specified by the choice of Ω_0 is assigned equally to each of the clusters and placed at the cluster centers. The gravitational field produced by this mass distribution is tabulated as a function of position in the region occupied by the test masses. The magnitude of the gravitational field as a function of time is scaled from linear perturbation theory, as discussed in § 2.3. This prescription provides the maximum tidal field that can reasonably be expected while keeping a consistent relation between luminous density and mass density both inside and outside the 3000 km s^{-1} volume. The true tidal field strength undoubtedly is somewhat less than what is given by this model; the exploration of other cases is left for future papers.

3.3. *Luminosity Density Calibration*

The global mean luminosity density relates the mass-to-light ratio, M/L, and the expansion time, t_0, to the cosmological parameters H_0 and Ω_0.

Our mean luminosity density is based on the Automatic Plate Measurement (APM) 1 in 20 redshift survey to $B_J = 17.15$ by Loveday et al. (1992), at median redshift 15,000 km s^{-1}. This new calibration samples a volume 30 times larger than the STP92 luminosity density calibration based on the Center for Astrophysics redshift survey to $m_{\rm Zwicky} = 14.5$ (Davis & Huchra 1982), so there is a considerably better chance now that we have a representative sample of the universe. The new calibration results in a 20% decrease from the STP92 value for the critical M/L in an Einstein–de Sitter universe.

Our procedure follows Efstathiou, Ellis, & Peterson (1988). A Schechter (1976) luminosity function fit to the APM data provides three parameters: the characteristic number density and faint-end power-law index,

$$\phi^* = 0.014\ h^3 \text{ galaxies Mpc}^{-3}\ , \quad \alpha = -0.97\ , \tag{10}$$

and the characteristic luminosity,

$$L_B^* = 1.28\ h^{-2} \times 10^{10}\ L_\odot\ , \quad M_B^* = -19.79 + 5 \log h\ . \tag{11}$$

The determination of L_B^* in the B_T system of the Revised Catalogue (de Vaucouleurs et al. 1991) is based on a transformation from the B_J photographic magnitude system specified by Efstathiou et al. (1988), $B_T = B_J - 0.29$.

The mean luminosity density is

$$\bar{\ell}_B = \phi^* L_B^* \Gamma(\alpha + 2)\ , \tag{12}$$

where the Γ is the gamma function. The above numbers give

$$\bar{\ell}_B = 1.76\ h \times 10^8\ L_\odot \text{ Mpc}^{-3}\ . \tag{13}$$

The critical mass density at $\Omega_0 = 1$ is

$$\rho_c = 2.78\ h^2 \times 10^{11}\ M_\odot \text{ Mpc}^{-3}\ , \tag{14}$$

whence the global mass-to-light ratio is

$$\rho_c/\bar{\ell}_B = 1580\ h\ M_\odot/L_\odot\ . \tag{15}$$

This number is on the B_T system but without absorption corrections, whereas these corrections are applied to our mass tracer catalog. The corrections amount in the mean to $0^m.20$ for inclination effects and $0^m.04$ for Galactic absorption in the domain of the APM survey with $|b| > 40°$. Finally, a correction of 0.979 is applied because our catalog has a luminosity cutoff of -16 mag. These adjustments produce a 22% increase in $\bar{\ell}_B$, so in our system of corrected $B_T^{b,i}$ the global mass-to-light ratio is

$$\rho_c/\bar{\ell}_B^{b,i} = 1290\ h\ M_\odot/L_\odot\ . \tag{16}$$

We have a check from the *IRAS* 1.9 Jy sample. The Yahil et al. (1991) estimate of the mean number density of sources is $\bar{n}_{IRAS} = 0.045\ h^3$ Mpc^{-3}, at their luminosity cutoff. Then the critical mass per *IRAS* source is

$$\rho_c/\bar{n}_{IRAS} = 6.2\ h^{-1} \times 10^{12}\ M_\odot\ . \tag{17}$$

For the *IRAS* sources within 3000 km s^{-1} with measured $B_T^{b,i}$ magnitudes, the optical luminosity per source is

$$\bar{\ell}_B^{b,i}/\bar{n}_{IRAS} = 4.7\ h^{-2} \times 10^9\ L_\odot\ . \tag{18}$$

The ratio of these two numbers,

$$\rho_c/\bar{\ell}_B^{b,i} \simeq 1300\ h\ M_\odot/L_\odot\ , \tag{19}$$

is in excellent agreement with the APM normalization in equation (16).

It is difficult to measure the mean luminosity density and evaluate the potential for systematic errors; our soft estimate is that equation (16) could be in error by 20%.

4. STATISTICAL MEASURES AND BIASES

We discuss here the procedure to obtain an unbiased distance measure and the χ^2 statistic we use to compare the measured distances with those predicted by a numerical solution for the orbits of the mass tracers. Here is a one-sentence summary of our procedures. The regression on *line widths* in a faint magnitude–limited calibrator sample provides the slope required to measure unbiased distances to individual galaxies in the field; errors are symmetric in the *logarithm*, so moduli are measured, and volume error scatter effects are minimized by evaluating *distances at observed velocities* rather than velocities at observed distances. Details follow.

4.1. *The Distance Estimator*

Several problems have been termed Malmquist bias (e.g., Teerikorpi 1984; Lynden-Bell et al. 1988; Tully 1989; Willick 1994). One arises because of the magnitude or diameter cutoffs that almost always limit samples (Malmquist 1922), another because distance errors tend to preferentially throw galaxies to smaller distances because more distant galaxies are more numerous (Malmquist 1920), and yet another because distance errors for the galaxies in a concentration masquerade as a converging peculiar velocity field. A common practice in the last decade has been to deal with such problems by the introduction of correction terms. This is a difficult art, however, in which even the sign of the correction can be in doubt, so we adopt and strongly advocate a different procedure in which one attempts to *neutralize* biases by using estimators that are likely to be close to unbiased, rather than seeking to correct for anticipated biases.

The two steps in the establishment of luminosity–line width distances with the method of Tully & Fisher (1977) are the calibration of the relation and the method of application. In our procedure the first step is to find the mean of the line width parameter as a function of the galaxy absolute magnitude rather than the mean absolute magnitude as a function of line width, that is, we use the so-called inverse rather than direct calibration. The alternative is liable to the 1922 Malmquist

bias. In the second step we use the observed galaxy apparent magnitude and line width to predict the distance modulus, which is compared to the model prediction. Since completeness is likely to be insensitive to line width at a given magnitude, our estimator of the distance modulus is unbiased, as desired.

To make these points more explicit we illustrate our procedure in the notation of Willick (1994) as follows. The line width parameter is

$$\eta = \log W_R^i - 2.5 , \tag{20}$$

where W_R^i is an inclination-corrected H I profile line width observable related to twice the maximum rotation velocity (Tully & Fouqué 1985). We assume that an absolute magnitude characteristic of galaxies with line width parameter η is given by the linear luminosity–line width relation

$$M = a - b\eta , \tag{21}$$

where a and b are constants.

Suppose the joint probability distribution in absolute magnitude and line width parameter in a fair volume-limited sample of galaxies is

$$dN = e^{-(\eta - a/b + M/b)^2/2\sigma(M)^2} F(M) dM\, d\eta . \tag{22}$$

The rms spread $\sigma(M)$ in η among the galaxies with given absolute magnitude M may depend on the value of M, and the function $F(M)$ takes account of the luminosity function and normalization. Equation (22) says the average value of η in a fair sample of galaxies with given M is

$$\langle \eta \rangle_M = (a - M)/b . \tag{23}$$

To calibrate the luminosity–line width relation expressed in this form one requires a fair sample of galaxies at known distances. To this end we use complete samples of galaxies in one or several clusters (specified for this study at the end of the section). With this calibration sample, a regression that minimizes the mean square scatter in η as a function of M yields the parameters a and b defined in equations (22) and (23).

The estimator of the distance modulus for a galaxy observed to have apparent magnitude m and line width parameter η is

$$\mu_e = m - a + b\eta = \mu + M - a + b\eta . \tag{24}$$

The last expression follows if the true distance modulus of the galaxy is μ. As Willick (1994) and others have clearly emphasized, this estimator is biased, when there is incompletion, in the sense that the expectation value of μ_e at given m and η is not equal to the true value μ. Furthermore, we cannot determine the amount of bias unless we have good models for $\sigma(M)$ and $F(M)$. But our dynamical analysis is not sensitive to the value of η, and we can assume that the selection of galaxies at given apparent magnitude m is not very sensitive to η. This independence from η means that for the purpose of the analysis of the peculiar velocity field we need the expectation value of our estimator for given m:

$$\langle \mu_e \rangle = \int dM\, d\eta\, F(M)(\mu + M - a + b\eta) e^{-(\eta - a/b + M/b)^2/2\sigma(M)^2} . \tag{25}$$

It follows from equation (23) that

$$\langle \mu_e \rangle = \mu . \tag{26}$$

That is, the estimator is unbiased. This is the quantity used in equation (28) to measure the goodness of fit of the model to the observations. We could reduce the statistical scatter in the measure in equation (28) if we corrected equation (24) to the expected value of the distance modulus μ at given η and m. The procedure does not seem advisable at our present state of knowledge, however, because an inadequate model for the correction would introduce a systematic error in the distance modulus.

Several features of this procedure might be noted and contrasted with other common practices. First, it is essential to our approach that the galaxies to which the estimator is applied are *statistically similar in properties to the calibrators*, with similar measurement uncertainties. These properties do not have to be specified beyond the definition of the slope and zero point of the regression to the calibrators, however. The completeness of the calibration sample in general will depend on the absolute magnitude M, but that requirement introduces no bias as long as the sample is large enough to determine the mean value of η as a function of M. As Willick (1994) points out, our calibration may be biased if galaxies are selected by diameter or by magnitude in a different passband from that of the distance estimator correlation, as almost inevitably is the case, and if line widths are correlated with galaxy surface brightnesses or colors. However, Willick's realistic simulations indicate that this bias is negligible in our sample, limited as we are to $cz < 3000$ km s^{-1}.

Our procedure is often called the inverse Tully-Fisher relation, and the expectation value of the absolute magnitude given η is called the forward relation.[1] The forward relation suffers the Malmquist (1922) bias in the domain where the scatter in the correlation overlaps the sample selection magnitude limit. In this domain, $\langle \mu_e \rangle < \mu$. The problem can be avoided by truncating the sample in line width or something correlated with line width (Bottinelli et al. 1986; Rood & Williams 1993; Lu, Salpeter, & Hoffman 1994) but at the cost of a substantial loss in sample size. If, instead, one attempts to correct for the bias (Teerikorpi 1984; Willick 1994), one must be able to specify the characteristics of the distance-dependent correlations. In particular, one must know the convolution of intrinsic and observational dispersions and the often subtle effects of sample selection. In our approach, on the other hand, *the onus of sample completion is transferred to the calibration.* As long as we are not inhibiting the sample with the measurements of line width, statistically unbiased distances are being measured over the full range of calibrated luminosities, whatever the degree of completion of the sample under study as a function of magnitude. We can use all observations of nonpathological galaxies and make a statistically unbiased distance estimate for each one.

The present preliminary study uses the calibration by Pierce & Tully (1988, 1992) based on a deep sample of Ursa Major Cluster galaxies. In future papers in this series, the calibration will be based on a more extensive three-cluster sample and applied to a much larger number of objects dispersed around the Local Supercluster.

4.2. *Volume Malmquist Bias*

Our strategy in building the dynamical model also differs from the more familiar practice in that our dynamical analysis is based on a redshift map rather than a map of the mass distribution in real space. The former approach, which has

[1] The terminology is curious, because R. B. T. has never advocated the use of what has come to be called the forward relation.

been taken also by Nusser & Davis (1994), has not been as widely discussed, so its hazards surely are not yet as well explored as the real space construction. We can note a very apparent advantage, however. Measurement errors distort either a real space or redshift map (Malmquist 1920; Lynden-Bell et al. 1988). For example, in a real-space map, if galaxies are uniformly distributed, then the volume effect causes more galaxies to be thrown forward by errors than thrown back. With available distance measurements the error in distance of a single galaxy is 15% to 20%. These large percentage errors cause a considerable distortion that grows linearly with increasing distance. By contrast, the scatter in our redshift catalog of mass tracers due to the small-scale motions we cannot model are expected to be 100 to 200 km s^{-1}, a 3% to 7% effect at 3000 km s^{-1} and constant in absolute terms with increasing distance.

4.3. *Velocity-Limited Volume Bias*

There is one significant deficiency to a velocity-limited sample as opposed to a distance-limited sample: the boundary of the sample volume is not spherical but rather depends on the peculiar velocity field we are computing. In the context of these calculations, missing regions of a sphere subtending the sampled volume effectively have density contrast $\delta\rho/\bar{\rho} = -1$, and this feeds back to cause accelerations that enhance the flattening. The result is that in early times the missing regions are inappropriately filled by mass tracers from the sample.

Distortion of the boundary arises from the peculiar velocities of the Local Group and at the sample boundary. The effect of Local Group peculiar velocity V_{LG} is to shift the edge of the sample at cutoff redshift cz_{max} to the distance

$$H_0 R = cz_{max} + V_{LG} \cos \phi , \quad (27)$$

where ϕ is the angle away from the direction of motion. Perpendicular to the peculiar velocity the sample boundary is at the appropriate distance, but in the direction of the Local Group motion it is V_{LG}/H_0 too distant, and behind the motion it is too near by the same amount. The off-centering of the Local Group is of no consequence, because we compute in center of mass coordinates. The problem is that the sample volume is deformed. Examples of possible shapes are presented in Figure 4. One sees that for values of $V_{LG}/cz_{max} < 0.5$ the departure from an offset sphere is quite small, so we do not have a significant problem, but we would have if we had chosen a cutoff redshift at $cz_{max} = 1000$ km s^{-1}.

As an aside, there are some curious effects with a sample boundary deformed by local motion. The sample volume is enlarged from the zero peculiar velocity case by the factor $(1+r^2)$, where $r = V_{LG}/cz_{max}$. An observer looking into the two hemispheres, in the direction of motion and away, sees volume effects that could be substantial. In the hemisphere of the motion, the volume is increased from the expected hemisphere volume by $(1 + 3r/2 + r^2 + r^3/4)$. In the other hemisphere, the volume is decreased by a factor of $(1 - 3r/2 + r^2 - r^3/4)$. This deformation can be important when determining luminosity functions and selection functions from galaxies in the Local Supercluster region. We have yet another reason to build an accurate model of the Local Supercluster.

A second cause of nonsphericity is the large-scale peculiar flow at the boundary. A concrete example of this problem arises with the circumstance that the center of mass of the Local Supercluster is distinctly offset within the 3000 km s^{-1} shell, with 3 times the light in the northern Galactic hemisphere as in the southern. The inward flow of the north Galactic pole boundary is greater than at the boundary in the opposite direction. Therefore, the redshift cutoff of the sample refers to a greater distance in the Virgo Cluster direction, which is near the north Galactic pole. Likewise, the tidal fields from large high-density regions outside the sample volume cause distortions. In some cases, the triple-value region of an external mass will be near the 3000 km s^{-1} boundary, so that the mass tracers beyond the external mass are thrown into the redshift range of our sample, and tracers which otherwise would be included are thrown out of the sample. This situation appears to actually be the case in the region near the Hydra and Centaurus clusters. However, in the current preliminary analysis very few galaxies with distance estimates are close to the boundary near the Hydra-Centaurus region, so inaccuracy in the detailed mass structure in that region does not significantly affect the tests.

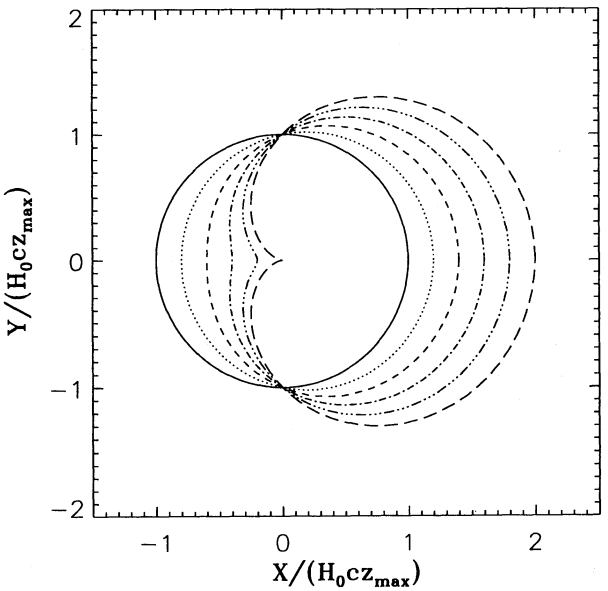

FIG. 4.—The boundary of a velocity-limited survey in a plane containing the peculiar motion of the observer. Different line types refer to ratios of peculiar velocity of the observer to the cutoff redshift of (0.0, 0.2, 0.4, 0.6, 0.8, and 1.0). In the case of the Local Group this ratio is approximately 0.1; hence, the distortion is minor though the origin is shifted.

The problems of a nonspherical boundary are greatly reduced by including the mass structures beyond the redshift cutoff. It does not matter if the mass tracers used in the dynamical computation are subject to an aspherical cutoff in distance if one can place external masses with sufficient accuracy to generate their proper contribution to the nearby peculiar flow. Placing objects with redshift $cz > 3000$ km s^{-1} at their Hubble flow distances should be satisfactory for the present purpose. However, the 3000 km s^{-1} discontinuity in the present models may be the greatest weakness of the current work, and we hope to give this issue closer attention in future papers.

4.4. *Test of the Fit of the Model to the Observations*

Our measure of the degree of consistency of the model prediction and the observations is the reduced χ^2 statistic

$$\chi^2 = \sum_{i=1}^{N} n_i \left(\frac{\mu_{m,i} - \mu_{TF,i}}{0.4} \right)^2 \Big/ \sum_{i=1}^{N} n_i . \quad (28)$$

Mass tracer i has n_i galaxies with distance measurements, the mean value of the measured distance moduli for mass tracer i is $\mu_{\mathrm{TF},i}$, and the model prediction for the distance modulus of the tracer is $\mu_{m,i}$. We have adopted a conservative estimate of the standard deviation in the measurement of an individual distance modulus, $\sigma(\mu) = 0.4$ mag. In the sample used in § 5, 186 mass tracers contain one or more galaxies with measured distances.

We use the distance modulus μ rather than the distance because the error in the luminosity–line width (Tully-Fisher) distance is symmetric in μ. We show in the next section that the scatter in $\mu_{m,i} - \mu_{\mathrm{TF},i}$ is not very sensitive to the redshift of the tracer and that the scatter is close to what is expected from the measurement error $\sigma(\mu)$. If, as this result indicates, χ^2 is dominated by the distance measurement error, then because the number of degrees of freedom is large, we can approximate the standard deviation in the value of χ^2 as

$$\sigma(\chi^2) = \left(2 \Big/ \sum_{i=1}^{N} n_i\right)^{1/2} = 0.08 , \qquad (29)$$

for the 289 galaxies with distance measurements used here.

A more commonly used measure of the goodness of fit is the mean square value of the difference $V_{\mathrm{obs}} - V_{\mathrm{model}}$ between measured and predicted velocities at a measured distance (Strauss 1989; STP92). Evaluation of a χ_V^2 statistic in this case requires the standard deviation of $V_{\mathrm{obs}} - V_{\mathrm{model}}$, which is the sum in quadrature of the measurement and model uncertainties. Since the latter depends on the value of the density parameter, an error in modeling the standard deviation of V_{model} as a function of Ω_0 can produce a systematic error in the value of Ω_0 at the nominal minimum of χ_V^2. The important point here is that the prediction of velocities as a function of position may be much more density sensitive, and hence subject to bias, than is the prediction of positions as a function of velocity.

5. NUMERICAL RESULTS

The computations presented here use the redshift catalog of 1138 mass tracers at $cz < 3000$ km s^{-1} described in § 3.1 and 289 luminosity–line width distance measurements listed in TSP92. We compare two cases, where, alternatively, the mass fluctuations external to the redshift catalog are neglected or are modeled by the distribution of Lauer-Postman Abell clusters described in § 3.2.

A specific example of the orbit solutions is shown in Figure 5. Only galaxies concentrated to the supergalactic plane are illustrated here. The diamonds denote positions today. The orbits of selected objects are indicated by the curved lines (comoving coordinates with respect to the sample center of mass). The Local Group, at the origin, the Virgo Cluster, and Ursa Major are identified by very thick lines. The other objects with identified orbits are all mass tracers associated with the Coma-Sculptor Cloud in the NBG nomenclature. This specific example is an illustration of a reasonable model, but it does not take into account the effects of masses beyond 3000 km s^{-1}. If distant masses are considered, then a dominant characteristic of the orbits is coherent streaming toward the minus Supergalactic-X (SGX) direction.

5.1. *Contour Maps of* χ^2

We have computed numerical action principle solutions at about 20 points in the $(M/L, t_0)$ plane and applied rescaling (§ 2.3) to double the resolution of this grid. The values of

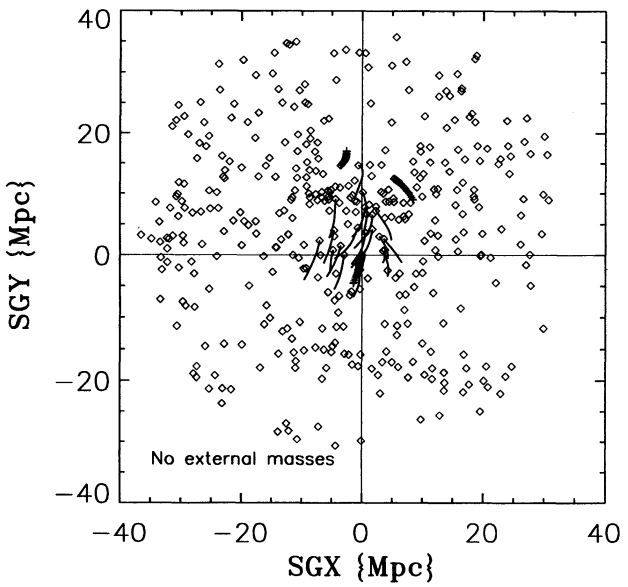

FIG. 5.—Action orbits. The model used for this illustration has $M/L = 200$, $t_0 = 9.7$ Gyr, and it excludes sources beyond 3000 km s^{-1}. The coordinates are supergalactic, and only tracers within ± 5 Mpc of the equatorial plane are plotted. Diamonds locate model positions today. Curved tails show the orbits of tracers drawn from the Coma-Sculptor Cloud (NBG catalog terminology). There are fat tails in the three cases of the Local Group (*at origin*), the Virgo Cluster (*upper left quadrant*), and the Ursa Major Cluster (*upper right quadrant*).

reduced χ^2 at each grid point are interpolated by a cubic polynomial fit at each t_0 value followed by a cubic spline fit at each M/L value to produce the contour maps of the reduced χ^2 statistic (eq. [28]) shown in Figure 6. In Figure 6*a* there are no external mass contributions. Figure 6*b* shows the effect of the external mass distribution as modeled by the Lauer-Postman sample of Abell clusters. The contour lines are placed at one standard deviation intervals (eq. [29]). The minimum values of χ^2 in the maps are close to unity: $\chi^2 = 1.29$ for no external masses and $\chi^2 = 1.17$ with the external mass model. These values are consistent with the proposition that the scatter between the model predictions and the observations is dominated by the distance measurement errors with some contribution from deficiencies in the model.

The axes of the figure are the free parameters in the computation of χ^2: the mass-to-light ratio M/L of the mass tracers and the expansion time t_0 of the cosmological model. If M/L in the region modeled by these mass tracers is consistent with the universal value, then we can use the measured global value, $M/L = 1290\ h\ \Omega_0$ (eq. [16]), to compute the cosmological parameters H_0 and Ω_0 as functions of t_0 and M/L. The dotted and dot-dashed lines in Figure 6 are loci of constant H_0 and Ω_0, respectively. The constraints placed on Ω_0 and the mass-to-light ratio, in the end, is quite similar to those from the linear analysis of STP92, as can be seen by comparing Figure 4 of that paper with this figure.

If the mass tracer catalog described a homogeneous and homogeneously expanding mass distribution, then the valley of the minimum of χ^2 would have a flat bottom along a line of constant rate of expansion of the system of mass tracers. The minimum of χ^2 in the valley and the twisting off of the constant rate of expansion result from the density fluctuations in the catalog. For small expansion ages, the masses become quite large along a line of constant rate of expansion. To avoid

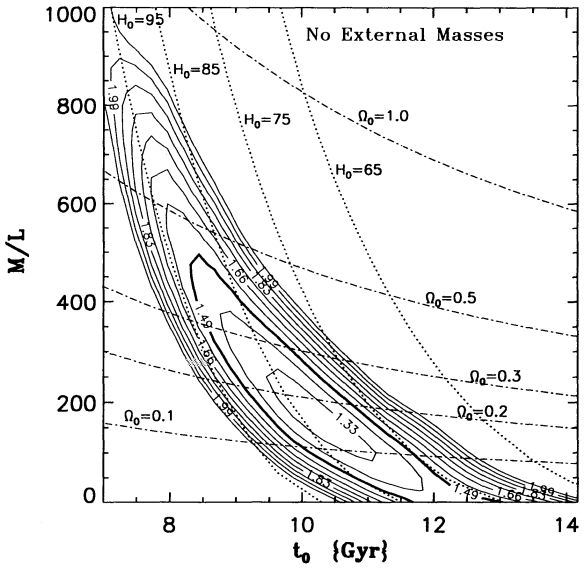

FIG. 6a

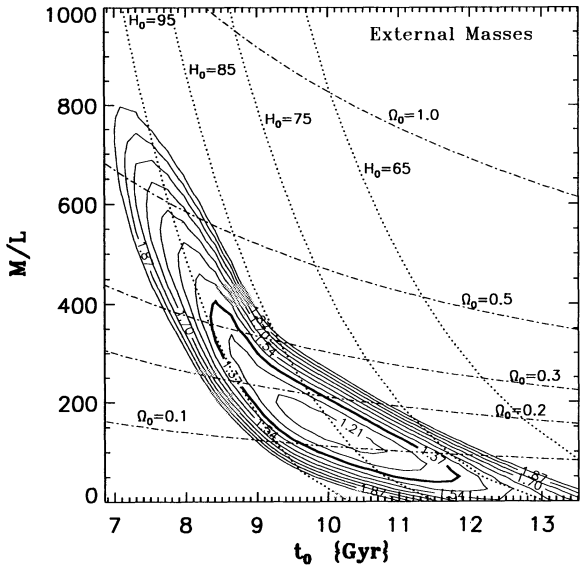

FIG. 6b

FIG. 6.—Contours of χ^2 as a function of the two free parameters M/L and t_0. This reduced χ^2 is calculated from the difference between model and observed distance moduli for 289 galaxies with luminosity–line width distance measurements. The normalization is given by the expected measurement error of $0^m.4$. Contours are at intervals of $0.08 \simeq 1\ \sigma$. The dashed line goes along the bottom of the minimum χ^2 valley. The lines of constant H_0 and Ω_0 are based on the Loveday et al. (1992) luminosity density normalization. (*a*) No external perturbation by masses beyond 3000 km s^{-1} distance. (*b*) External perturbation modeled by the distribution of the great clusters.

excessive peculiar motions, the best models must shift to lower mass-to-light ratios and thus to higher values of H_0.

For the case where external masses are neglected, Figure 7*a* displays the minimum value χ^2 as a function of t_0 (*dashed curve, right-hand scale*) and the value of M/L at the minimum χ^2 as a function of t_0 (*solid curve, left-hand scale*). The latter is usefully approximated as

$$M/L = 1100 \exp\,[(7 - t_0)/2.2] - 100\ . \qquad (30)$$

At 1 σ from the minimum of χ^2 the parameters are

$$9.0 < t_0 < 11.5\ \text{Gyr}\ , \quad \Omega_0 = 0.17 \pm 0.10\ . \qquad (31)$$

The effect of the model for the external masses is shown in Figure 7*b*. The minimum of χ^2 drops by about 1 σ, the valley shifts to an empirical fit of

$$M/L = 900 \exp\,[(7 - t_0)/2] - 50\ , \qquad (32)$$

and the 1 σ range shifts to

$$9.0 < t_0 < 11.0\ \text{Gyr}\ , \quad \Omega_0 = 0.15 \pm 0.08\ . \qquad (33)$$

When the external mass model is applied, the curvature of the floor of the χ^2 valley is larger, so high and low values of M/L are more strongly excluded.

If t_0 is required to be no less than 11 Gyr, which seems to be a very conservative bound from stellar evolution and radioactive decay ages, then the solutions require that the density parameter is not much larger than about $\Omega_0 = 0.1$ because the Hubble parameter is not less than about 80 km s^{-1} Mpc^{-1}. The expansion time issue is discussed further in § 5.5.

In our model the major part of the tidal field of the external masses on the mass tracers comes from the nearest superclusters, Hydra-Centaurus and Perseus-Pisces at $cz = 3500$ and 5500 km s^{-1}. These two superclusters are situated on opposite sides of the sky near the Galactic plane. The Virgo Cluster is only 15° from the north Galactic pole and therefore is nearly perpendicular to the axis connecting the nearest adjacent superclusters. The Local Group thus experiences tidal contraction toward Virgo. To counter this effect and preserve a reasonable value for the peculiar motion of the Local Group and neighboring groups toward the center of the Local Supercluster, one must either reduce the mass density in the Virgo region or reduce the age of the universe. We interpret this tidal effect as the cause of the tighter constraint on M/L and Ω_0 when the external mass model is applied.

5.2. *Observed and Model Distances*

Figures 8, 9, and 10 show scatter plots of the residual differences $\Delta\mu$ between observed and model distance moduli as a function of the redshift of the mass tracer. Figure 8 presents a case near the minimum χ^2 for no external masses. Here and along the χ^2 minimum valley, the residuals of $\Delta\mu$ consistently trend downward with increasing redshift cz. The trend is reduced if the mass-to-light ratio is increased, but at the expense of making the model distances systematically larger than the observations. We expected (Shaya, Peebles, & Tully 1994) that the problem would be relieved by the addition of external masses: it was reasoned that the correlation of $\Delta\mu$ with cz is an indication of excess overdensity at large Virgocentric distances when the density is about right in the local neighborhood. As we noted in the last subsection, the external masses cause tidal compression between us and the Virgo cluster, which allows a lower local mass density. In Figure 9, for the external masses near the χ^2 minimum at $t_0 = 9.8$ Gyr with $M/L = 160$, the trend of $\Delta\mu$ with cz is reduced, consistent with this reasoning. Figure 10 shows the external mass case with $t_0 = 8.0$ Gyr with $M/L = 500$, which is in the χ^2 valley but approximately 4 σ from the best value. One is struck by the subtlety of the differences between the scatter plots in these large and small Ω_0 cases. However, when these plots are placed one over the other, one sees that the scatter is consistently greater in Figure 10, as the reduced χ^2 indicates.

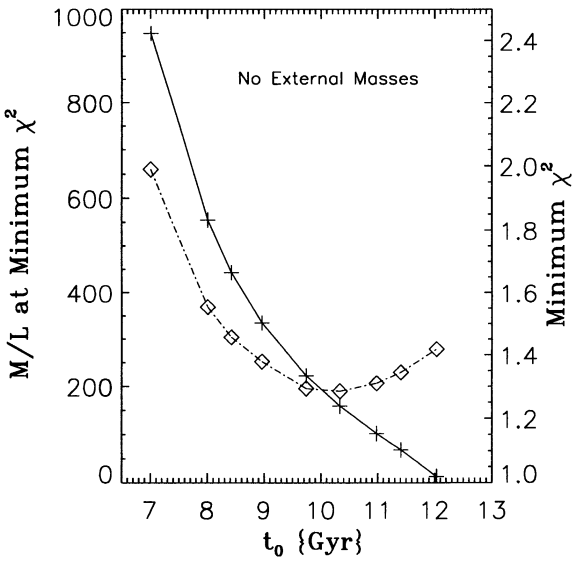

FIG. 7a

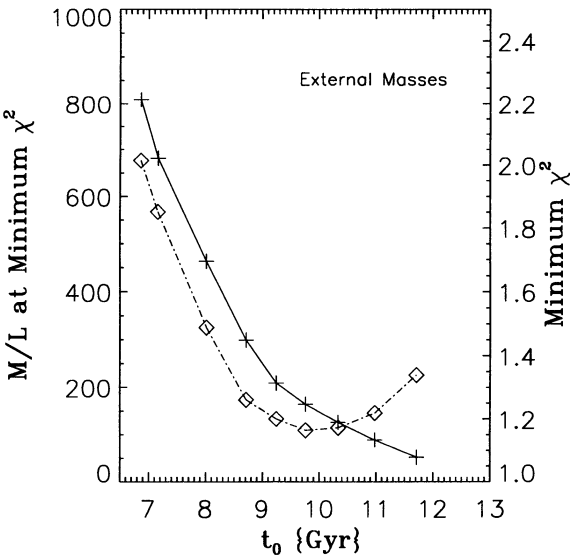

FIG. 7b

FIG. 7.—Minimum reduced χ^2 as a function of time (*dashed line, read from right axis*), and M/L ratio at the minimum χ^2 (*solid line, read from left axis*). These values track the floor of the χ^2 valley in the previous figure. (*a*) No external sources considered. (*b*) External sources taken into account. In this latter case, the χ^2 minimum is deeper and better defined.

5.3. *Observed and Predicted Peculiar Velocities*

Figure 11 shows a scatter plot of observed peculiar velocities $U_{\rm obs} = cz - H_0 D_{\rm TF}$ for the mass tracers with luminosity–line width distances against the model peculiar velocities $U_m = cz - H_0 D_m$, where D_m is the model prediction of the distance. The model is near the χ^2 minimum with external masses ($M/L = 160$ and $t_0 = 9.8$). Although our analysis is independent of H_0, we must choose a specific value to derive peculiar motions, so we have chosen 90 km s^{-1} Mpc^{-1} to be consistent with the APM survey luminosity density normalization and this mass-to-light ratio. The correlation coefficient is 0.42, and the probability of obtaining a higher value with 186 data points from a random distribution is well below 1%. However, a high correlation coefficient is not necessarily proof of a true correlation because if one chooses a sufficiently low value for H_0, one is guaranteed a strong correlation (the correlation coefficient goes to unity as H_0 goes to zero). To the extent that one believes 90 is not a low value for H_0, one can believe that this figure indicates that peculiar velocities actually have something to do with gravitational influences acting over time.

A regression based on equal errors on the two axes would result in a slope significantly greater than unity and would imply that the model considerably underestimates the peculiar

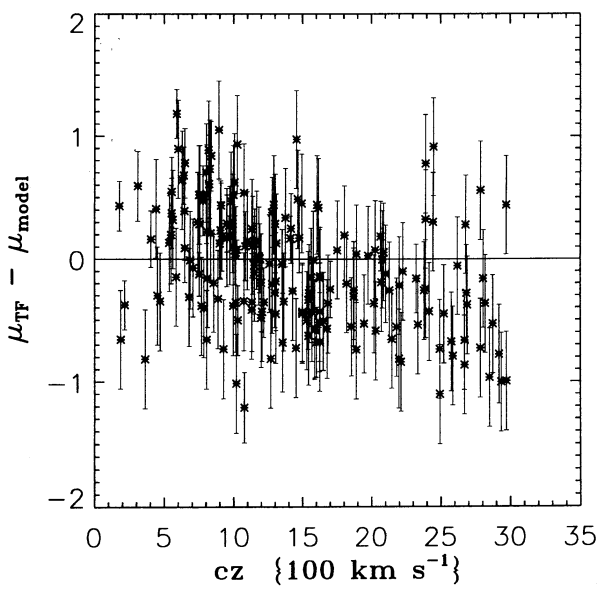

FIG. 8.—Observed minus model distance moduli vs. redshift for a model without external sources. In this case, $M/L = 150$, and $t_0 = 10.3$. There tends to be a systematic decrease toward higher cz. If M/L choices are too high or too low, the points systematically shift down or up, respectively.

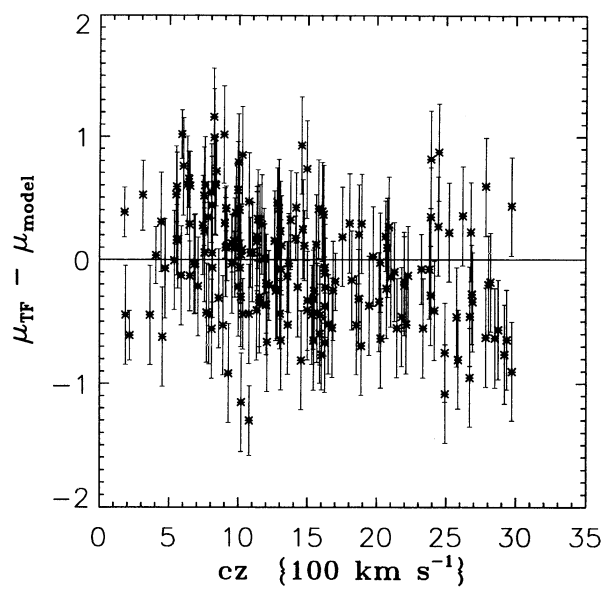

FIG. 9.—Observed minus model distance moduli vs. redshift including external sources. Now, systematics are significantly reduced. $M/L = 160$, $t_0 = 9.8$, and $\chi^2 = 1.20$.

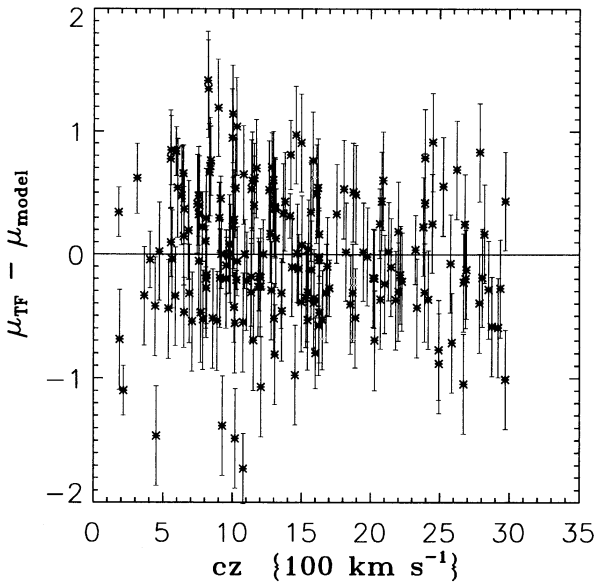

FIG. 10.—Observed minus model distance moduli vs. redshift including external sources but at a higher M/L choice along the minimum χ^2 valley. $M/L = 500$, $t_0 = 8.0$, and $\chi^2 = 1.54$. The rms scatter is consistently larger than that in Fig. 9.

velocities. This analysis could be very misleading, however. The errors in the observed peculiar velocities are dominated by the errors in the distance measurements, which amount to 600 km s^{-1} at the edge of the sample, and are comparable to or larger than the expected true peculiar velocities. The numerical action model is expected to do better because it is, at least, likely to get the sign of the peculiar velocity correct most of the time in predicting that galaxies tend to fall in toward regions of neighboring high galaxy density. Consistent with this argument, we have the evidence from the preceding subsection that the distance modulus residuals are dominated by the errors in the measured distance moduli. It follows that a less biased regression would minimize the errors in the observed quantities as a function of the model prediction. As indicated in the figure, the slope of this regression fit is close to unity.

Figure 12 shows the data in Figure 11 another way, as a scatter plot of observed minus model peculiar velocity as a function of the predicted peculiar velocity of the mass tracer. This plot may be a useful way to identify systematic errors in the model. In particular, a few large deviations, including three groups excluded from the analysis because they would lie off the plot region, are in the direction of the infall region around the Virgo Cluster. These mass tracers are not placed near the positions we expected based on our earlier work on infall into the Virgo Cluster (Tully & Shaya 1984), but they would be if we increased the mass-to-light ratio of the Virgo Cluster relative to the mass tracers in less dense regions. We have run a few trials in which a larger value of M/L is assigned to the mass tracers associated with the richest clusters. The indications are that the resulting increased sizes of the triple-value regions create alternative positions for the mass tracers that are in better agreement with the measured distances. We hope to present a detailed analysis of this issue in a separate paper.

The positive correlation of observed and peculiar velocities in Figure 11 is evidence that the peculiar velocities are being observed in a statistical sense, and the correlation coefficient is about right if, as we have argued, the scatter in the measured peculiar velocities is dominated by the distance errors. This comparison of observed and predicted peculiar velocities is commonly used as a test of models for the deviations from pure Hubble flow and indeed was the main statistical measure in the early stages of our program. The difficulty of dealing with the mix of measurement errors and the Ω_0 dependence of model velocities has led us to prefer the rms difference of predicted and observed distance moduli.

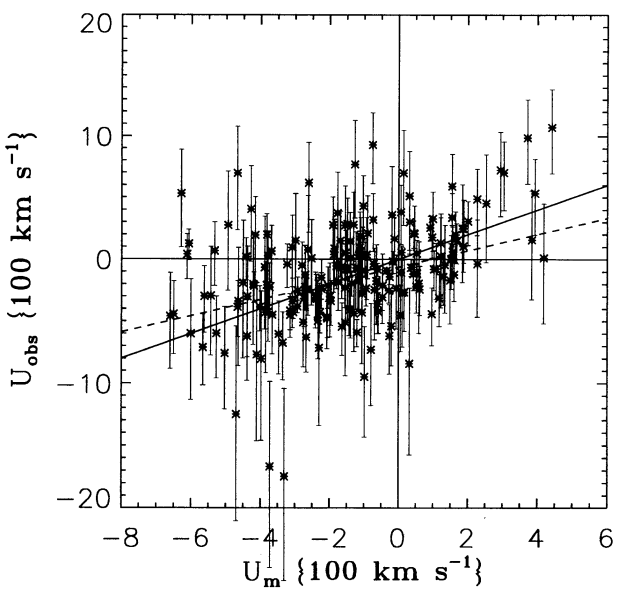

FIG. 11.—Observed peculiar velocities ($U_{obs} = cz - H_0 D_{TF}$) vs. model peculiar velocities ($U_m = cz - H_0 D_m$) for the case with $\Omega_0 = 0.10$ and $H_0 = 90$ and with external masses included. A linear regression fit (*dashed line*) is made with errors in the observed quantities. The oblique solid line is where $U_{obs} = U_m$. Errors are derived from an assumed rms uncertainty of 0^m.4 in an individual distance modulus. The axes have different scales to accommodate the much greater scatter in the observed quantities.

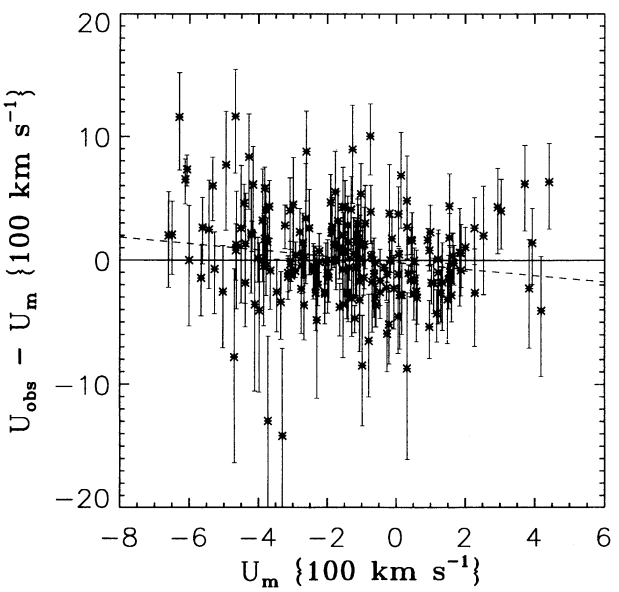

FIG. 12.—Observed minus model peculiar velocities vs. model peculiar velocities. This plot provides another way of viewing the data of the previous figure. The regression fit (*dashed line*) is close to horizontal, as it should be for a good model.

5.4. *The Local Density Contrast*

As the mass-to-light ratio is increased, the model distances generally increase to maintain the required match with the observed redshifts and avoid excess infall velocities into the Virgo Cluster and the Local Supercluster in general. The result is a decrease in the local luminosity density relative to the global mean. In the same way, an increase in t_0 increases the distances because increased expansion time with given masses also tends to increase the inward peculiar velocities. The valley of the minimum of χ^2 is established by the tradeoff between an increase in t_0 and a decrease in the mass-to-light ratio: densities and distances remain close to optimal when compared with the measurements of distances. Figure 13 gives examples of these trends in terms of the effective luminosity density profile. The origin of this figure is at the Local Group, and the model output distances are used to specify the mean luminous density within a given distance from the Local Group. The horizontal lines show the APM global mean luminosity density. The solid line shows a model at the minimum of χ^2, with $H_0 = 85$, $\Omega_0 = 0.2$, $M/L = 200$, and no external masses. Here the region remains slightly overdense to the edge of the sample just beyond 30 Mpc. In the case with the lowest density contrast (*long-dashed line*), the value of M/L has been increased to 800, while t_0 was unchanged. In the model with the highest density contrast (*triple-dot–dashed line*) the mass-to-light ratio has been lowered to $M/L = 45$, and t_0 was again unchanged. The other two cases are on the minimum valley of χ^2, with $\Omega_0 = 0.044$ and $M/L = 45$ (*dotted line*) and $\Omega_0 = 0.42$ and $M/L = 475$ (*short-dashed line*). They show, as expected, similar density profiles, with only minor readjustments in distances of specific features.

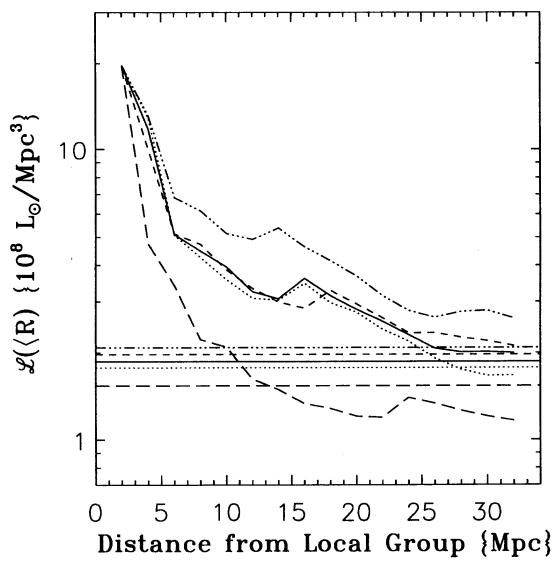

FIG. 13.—Cumulative luminosity density profiles as a function of distance from the Local Group. The horizontal lines with the same type style show the mean luminosity density (which differs between models, depending on H_0). The solid curve corresponds to a case near the minimum of χ^2: $M/L = 200$ and $t_0 = 9.7$ Gyr. Here the luminosity density just approaches the global mean at the edge of the sample region. The situation is similar with other cases near the χ^2 minimum valley (*dotted curve*: $M/L = 45$ and $t_0 = 11.4$ Gyr; *short-dashed curve*: $M/L = 475$ and $t_0 = 8.4$ Gyr). In models off the χ^2 minimum valley the luminosity density can fall more quickly (*long-dashed curve*: $M/L = 800$ and $t_0 = 9.7$ Gyr) or more slowly (*dash-dotted curve*: $M/L = 50$ and $t_0 = 9.7$ Gyr).

5.5. *The Expansion Time Problem*

The fit of our model to the distance measurements requires an expansion time t_0 near 10 Gyr, consistent with a Hubble constant in the range of 80 to 90 km s^{-1} Mpc^{-1}. Since this value for the expansion time seems uncomfortably short, we mention three possibilities often mentioned to increase the age. First, physical lengths and times in our computation are tied to the distances assigned to the luminosity–line width calibrators. If these distances were multiplied by the factor α, it would multiply the expansion time by the same factor (eqs. [6] to [9]). The leeway for adjustment here seems to be only about 10%–15%, however, because our distance scale is consistent with other recent measurements (Jacoby et al. 1992; Freedman et al. 1995). Second, the age difficulty has motivated consideration that we live in a very large low-density region, which would make the global value of H_0 significantly lower than the locally measured effective value (Turner, Cen, & Ostriker 1992). However, the parameter we directly measure is t_0, not H_0, so the normalization of H_0 does not affect our ages. Third, if the density parameter Ω_0 is less than unity a cosmological constant that makes the universe cosmologically flat increases the expansion time relative to an open universe with the same value of Ω_0.

In a preliminary exploration of this possibility we computed a grid of solutions with nonzero Λ by incorporating the appropriate variant of equation (2). The values of χ^2 as a function of M/L and Ω_0 are remarkably similar to the open model case. That is, there is the indication that our constraints on Ω and M/L would be little changed if one used a cosmological constant to increase the age of the universe and make the universe flat and consistent with the standard picture for inflation. However, if $\Omega_0 = 0.2$ (0.1), then the age of the universe is only increased by 26% (41%). If the distance scale zero point is unchanged, flat universe models with $\Omega_0 > 0.1$ have $t_0 < 15$ Gyr.

5.6. *Motion of the Local Group*

The peculiar velocity of the Local Group that arises in the models may be compared to the motion of the Local Group deduced from the dipole of the cosmic microwave background. The large plus sign in Figure 14 shows the motion of the Local Group with respect to the cosmic microwave background reference frame in supergalactic coordinates. The solid curve shows the motion of the Local Group in our model for solutions in which the external masses are neglected, and the dashed curve shows the effect of adding the external masses. The parameters are in the valley of the minimum of χ^2; the solutions are labeled by the expansion time t_0. Without external masses, one sees the influence of the Local Supercluster on the peculiar motion of the Local Group. For one of the best models with external masses, where $t_0 = 9.2$ Gyr and $M/L = 250$, the peculiar velocity of the Local Group in supergalactic coordinates is $(-346, 96, -744) = 763$ km s^{-1} to right ascension $\alpha = 8^h15^m$ and declination $\delta = -33°5$, while the microwave background dipole velocity is $(-318, 315, -348) = 567$ km s^{-1} to $\alpha = 10^h33^m$, $\delta = -24°0$ (Bennett et al. 1994, with solar motion 250 km s^{-1} to $l = 90$, $b = 0$). It is actually reassuring that the model amplitude is greater than the actual amplitude because the maximal tidal field model was used. One possible prescription to correct the model would be to (1) decrease the effective masses of the clusters by about 30%, (2) double the mass for the Virgo Cluster to increase the SGY component, and (3) decrease the influence of the Pisces

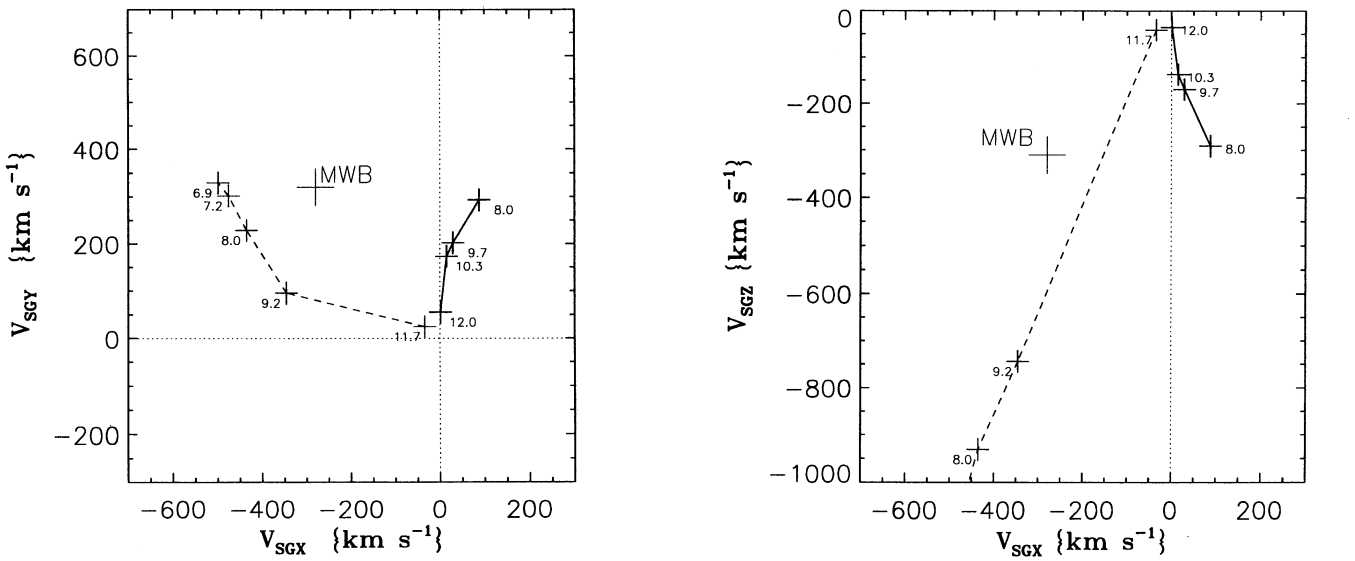

FIG. 14.—Two projections of the peculiar velocity of the Local Group in supergalactic coordinates. Solid lines connect results from models along the χ^2 minimum valley in the case of no external masses; dashed lines connect results with external masses. Each plus sign represents the result from a specific model, identified by the value of the expansion time t_0. The large plus signs show the motion of the Local Group with respect to the microwave background radiation.

and Perseus Clusters by about 25% to increase the negative SGX component and to decrease the negative SGZ component. Of course, many other prescriptions are possible. It is also reasonable that inhomogeneities beyond 15,000 km s^{-1} contribute significantly to the Local Group motion. With our present study, we have only made a preliminary, naive foray into the problem of large-scale contributions and the microwave background constraints.

6. DISCUSSION

We comment here on three issues we hope to be able to address in more detail in future papers in this series.

6.1. *Biases in Measurements and Models*

Our aim in this analysis of the departures from pure Hubble flow has been to set up the methodology of the astronomical measurements, the model computations, and the statistics that compare the two, so that we have made the biases tolerably small and not in need of corrections. The dynamical model predicts the distances of mass tracers given their angular positions, redshifts, apparent magnitudes, mass-to-light ratios, and the expansion time of the cosmological model. The predicted distance moduli μ_m are compared to astronomical measurements arranged so that the bias in the measured values μ_{TF} is likely to be small. Perhaps the major issue here is whether the cluster members used in the calibration are indeed statistically similar to the galaxies in groups and associations. A test that provides some confirmation is the reasonable agreement in the form of the calibration when separate clusters are evaluated. This consistency will be discussed in connection with the three-cluster calibration that will be used in future work. Another test is the consistency of the residuals $\mu_{TF} - \mu_m$ in clusters and the field. The indication from Figure 9 is that the scatter in $\mu_{TF} - \mu_m$ is about what would be expected from measurement errors that are insensitive to distance or environment. There is a systematic trend of the residuals with distance which we are inclined to attribute to two effects: the gravitational field of large-scale mass fluctuations and a higher value of M/L in the neighborhood of the Virgo Cluster. One of the goals for future papers in this series will be the study of these two effects with the denser set of 900 distance measurements now available.

Our program is complementary to the approach taken in the *IRAS*/POTENT analysis (Bertschinger et al. 1990; Dekel et al. 1993), in which one predicts the mass distribution as a function of position from peculiar velocity measurements and the Hubble and density parameters. The results from these latter studies give preference for a value of the density parameter in the range $0.6 < \Omega_0 < 1.3$. The procedure starts from a map of the velocity field that is noisy because of measurement uncertainties and requires substantial corrections for biases and heavy smoothing. The POTENT corrections have been very carefully tested in N-body models, however, and it would be exceedingly useful to subject our approach to similar scrutiny. We have recently begun this important exercise.

It is worth emphasizing that a value of the density parameter near $\Omega = 0.4$ would not strongly violate the constraints from either approach. Since the POTENT analysis is, of necessity, applied to a larger region, the results are quite reconciled if there are density fluctuations on scales greater than 3000 km s^{-1} that would not affect our analysis. Given the great differences in methodologies, the degree of consistency of results from the two approaches is encouraging. Continued comparison between the two methods should provide valuable insight into the nature of the large-scale mass distribution and the total matter content of the universe.

6.2. *Mass Bias and the Numerical Action Method*

If there is a significant mass component that is more smoothly distributed than our mass tracers, it will not be fairly measured by the relative motions of nearby mass tracers, and the computation therefore will underestimate the mean mass density. Branchini & Carlberg (1994) and Dunn & Laflamme (1995) give specific examples of this effect in the biased cold dark matter (CDM) cosmogony. This cosmogony predicts that large galaxies have overlapping halos. The result is very clearly illustrated in Figure 5 of Branchini & Carlberg (1994), which

shows that for their choice of parameters in the CDM cosmogony the effective mass derived from the relative motions of galaxy pairs at a separation of approximately 1 Mpc is only about 20% of the total within 5 Mpc of the pair, while at a separation of approximately 2 Mpc the effective mass is close to the mass within 5 Mpc. These numbers depend on the shape and normalization of the mass fluctuation power spectrum, but the effect surely is generic to the picture. However, the effect is contrary to the evidence from the redshifts of the galaxies in and near the Local Group. Zaritsky et al. (1989) point out that if the radial velocities of the dwarf spheroidal galaxy Leo I at 200 kpc from the Milky Way and the Andromeda Nebula at 700 kpc distance are the result of the gravitational assembly of the Local Group, then the mass-to-light ratio of the two dominant group members, the Milky Way and M31, is $M/L \sim 100$ solar units, and the mass of the Milky Way is concentrated within a radius of approximately 200 kpc, contrary to the prediction of the CDM cosmogony. The same result follows from the computation of orbits by the numerical action method (Peebles 1995). The action solutions also indicate that the redshifts of the neighboring groups of galaxies, at distances $r \sim 3$ Mpc, require a similar value of the mass-to-light ratio (P94). That is, the evidence is that most of the mass in the nearby groups is concentrated in relatively compact halos. There is no room for substantially more mass in halos extending to 1 Mpc.

In any event, our mass tracers are groups of galaxies defined by a procedure that minimizes the biases identified by Branchini & Carlberg (1994) and Dunn & Laflamme (1995). By construction, none of our mass tracers should have intersected: they are either moving apart or approaching one another for the first time. Hence, there should be negligible overlapping halos, even if, contrary to the evidence from the nearby region, galaxies have halos that extend beyond 1 Mpc radius.

Perhaps some other form of dark matter has a broader coherence length, so it is not detected in relative motions on scales of a few megaparsecs. If so, we may hope to detect it in more detailed sampling of the peculiar motions within 3000 km s^{-1}. The present indications are in the opposite direction, however, suggesting that M/L is larger in the most dense regions. That is, the mass distribution can be more strongly clustered than the galaxies, rather than smoother, at least in some circumstances. It is also remarkable that the value of the mass-to-light ratio estimated in this much larger scale study is so similar to the mass-to-light ratio obtained in the above studies of individual groups of galaxies.

Our use of the action principle assumes that each galaxy or group of galaxies in a mass tracer has behaved as a particle back to a time when the galaxy peculiar velocities were much smaller than they are now. If two galaxies merged at low redshift, the assumption can still be a good approximation when applied to the motion of the center of mass of the material now in the single galaxy, if the two parts originated at neighboring comoving positions. Our use of mass tracers that contain several galaxies simply extends the merging to a larger scale. Although we did not set out directly to test the effect of this merging, we can report the following experience. In early computations we used a lower density threshold for the assignment of galaxies to mass tracers, so that we had approximately half the number of mass tracers in the present sample. This coarser sampling yielded very similar orbits and numerical values for χ^2 as a function of M/L and t_0. Future computations with faster machines and more efficient variational techniques may allow another test based on finer sampling. If the mass tracers are smaller, we will have to deal with a larger number of triple-value and multiple-value regions. This investigation can be done, perhaps following the method in Peebles (1995), but it will be a demanding computation. Perhaps a better short-term hope for a more complete test is the use of realistic N-body simulations, as in the analysis by Branchini & Carlberg (1994) of a nearly unbiased numerical simulation. It will be possible to test for the effects of nonspherical mass tracers, possibly an important consideration at early times, and for the influence on the determination of Ω_0 of what Dunn & Laflamme (1995) call the "orphan" particles of a CDM-type model, the most weakly clustered component.

6.3. *Large-Scale Mass Fluctuations*

Our generalization of the numerical action method to take account of large-scale (>3000 km s^{-1}) density fluctuations by an imposed gravitational field that evolves in accordance with perturbation theory is meant to probe the nature of the large-scale density fluctuations and to remedy the aspherical discontinuity resulting from the redshift cut in the sample of mass tracers. In the numerical results shown in § 5, the application of the gravitational field of an external mass distribution modeled as the distribution of the Abell clusters actually improves the consistency of the computed orbits with the observations. There is a delicate balance, however, because with such large mass assigned to each cluster, a small change in position of one of the nearer ones can have a large influence on the orbits of the mass tracers. A better model would put some fraction of the mass in the great clusters and the rest at, say, the positions of *IRAS* galaxies. We will investigate such a model in the next phase of our study. It will be interesting to see whether a believable measurement of this mass fractionation between great clusters and spirals can be derived from the behavior of the χ^2 statistic.

We thank the following people for making digital versions of their catalogs available to us: Marc Davis and Michael Strauss for the 1.9 Jy *IRAS* Survey, Nick Kaiser for the binned 1 in 6 0.6 Jy *IRAS* survey, Tod Lauer and Marc Postman for their Abell cluster sample, and especially Amos Yahil and Karl Fisher for a prerelease version of the 1.2 Jy *IRAS* survey, from which we extracted sources with $cz < 3000$ km s^{-1}. We thank Adrian Melott for discussions. This research was supported in part by grants from the National Science Foundation and at Caltech by the Fairchild Distinguished Scholar Program.

REFERENCES

Abell, G. O. 1958, ApJS, 3, 211
Abell, G. O., Corwin, H. G., Jr., & Olowin, R. P. 1989, ApJS, 70, 1
Bennett, C. L., et al. 1994, ApJ, 436, 423
Bertschinger, E., Dekel, A., Faber, S. M., Dressler, A., & Burnstein, D. 1990, ApJ, 364, 370
Bottinelli, L., Gouguenheim, L., Paturel, G., & Teerikorpi, P. 1986, A&A, 156, 157
Branchini, E., & Carlberg, R. G. 1994, ApJ, 434, 37
Davis, M., & Huchra, J. P. 1982, ApJ, 254, 437
Dekel, A., Bertschinger, E., Yahil, A., Strauss, M., Davis, M., & Huchra, J. 1993, ApJ, 412, 1
de Vaucouleurs, G., de Vaucouleurs, A., Corwin, H. G., Jr., Buta, R. J., Paturel, G., & Fouqué, P. 1991, Third Reference Catalogue of Bright Galaxies (New York: Springer)
Dressler, A., Lynden-Bell, D., Burstein, D., Davies, R. L., Faber, S. M., Terlevich, R. J., & Wegner, G. W. 1987, ApJ, 313, 42
Dunn, A. M., & Laflamme, R. 1993, MNRAS, 264, 865
———. 1995, preprint

Efstathiou, G., Ellis, R. S., & Peterson, B. A. 1988, MNRAS, 232, 431
Fisher, K. B. 1992, Ph.D. thesis, Univ. of California, Berkeley
Fisher, K. B., Strauss, M. A., Davis, M., Yahil, A., & Huchra, J. P. 1992, ApJ, 389, 188
Freedman, W. L., et al. 1995, Nature, 371, 757
Jacoby, G. H., Branch, D., Ciardullo, R., Davies, R. L., Harris, W. E., Pierce, M. J., Pritchet, C. J., Tonry, J. L., & Welch, D. L. 1992, PASP, 104, 599
Kaiser, N., Efstathiou, G., Ellis, R., Frenk, C., Lawrence, A., Rowan-Robinson, M., & Saunders, W. 1991, MNRAS, 252, 1
Lauer, T. R., & Postman, M. 1994, ApJ, 425, 418
Lilje, P., Yahil, A., & Jones, B. J. T. 1986, ApJ, 307, 91
Loveday, J., Peterson, B. A., Efstathiou, G., & Maddox, S. J. 1992, ApJ, 390, 338
Lu, N. Y., Salpeter, E. E., & Hoffman, G. L. 1994, 426, 473
Lynden-Bell, D., Faber, S. M., Burstein, D., Davies, R. L., Dressler, A., Terlevich, R. J., & Wegner, G. W. 1988, ApJ, 326, 19
Malmquist, K. G. 1920, Medd. Lunds Ast. Obs. Ser. II, No. 22
———. 1922, Medd. Lunds Ast. Obs. Ser. I, No. 100
Nusser, A., & Davis, M. 1994, ApJ, 421, L1
Peebles, P. J. E. 1989, ApJ, 344, L53 (P89)
———. 1990, ApJ, 362, 1 (P90)
———. 1994, ApJ, 429, 43 (P94)
———. 1995, ApJ, 449, 52
Pierce, M. J., & Tully, R. B. 1988, ApJ, 330, 579
———. 1992, ApJ, 387, 47
Rood, H. J., & Williams, B. A. 1993, MNRAS, 263, 211
Rowan-Robinson, M., Saunders, W., Lawrence, A., & Leech, K. J. 1990, MNRAS, 253, 485
Schechter, P. L. 1976, ApJ, 203, 297
Shaya, E. J., Peebles, P. J. E., & Tully, R. B. 1994, in Cosmic Velocity Fields: 9th IAP Astrophys. Meeting, ed. F. R. Bouchet & M. Lachieze-Rey (Paris: Editions Frontières), 393
Shaya, E. J., Tully, R. B., & Pierce, M. J. 1992, ApJ, 391, 16 (STP92)
Strauss, M. A. 1989, Ph.D. thesis, Univ. of California, Berkeley
Strauss, M. A., Yahil, A., Davis, M., Huchra, J. P., & Fisher, K. 1992, ApJ, 397, 395
Teerikorpi, P. 1984, A&A, 141, 407
Tully, R. B. 1987, ApJ, 321, 280
———. 1988a, Nearby Galaxies Catalog (New York: Cambridge Univ. Press) (NBG Catalog)
———. 1988b, AJ, 96, 73
———. 1989, in ASP Conf. Proc 100, The Extragalactic Distance Scale, ed. S. van den Bergh & C. J. Pritchet (Provo: Brigham Young Univ. Press), 318
Tully, R. B., & Fisher, J. R. 1977, A&A, 54, 661
Tully, R. B., & Fouqué, P. 1985, ApJS, 58, 67
Tully, R. B., & Shaya, E. J. 1984, ApJ, 281, 31
Tully, R. B., Shaya, E. J., & Pierce, M. J. 1992, ApJS, 80, 479 (TSP92)
Turner, E. L., Cen, R., & Ostriker, J. P. 1992, AJ, 103, 1427
Willick, J. A. 1994, ApJS, 92, 1
Yahil, A., Strauss, M. A., Davis, M., & Huchra, J. P. 1991, ApJ, 372, 380
Zaritsky, D., Olszewski, E. W., Schommer, R. A., Peterson, R. C., & Aaronson, M. A. 1989, ApJ, 345, 759